UTD Shooting-and-Bouncing Extension to a PO/PTD Ray Tracing Algorithm

F. Weinmann

Research Institute for High Frequency Physics and Radar Techniques, FGAN E.V.
Neuenahrer Str. 20, 53343 Wachtberg, Germany, weinmann@fgan.de

Abstract **–** This paper deals with the efficient combination of three well-established electromagnetic modeling methods, a Shooting-and-Bouncing-Rays (SBR) algorithm on the basis of the Geometrical Optics (GO), a source-based calculation of scattered field strengths using Physical Optics (PO) and Physical Theory of Diffraction (PTD), and diffraction calculation on the basis of the Uniform Theory of Diffraction (UTD). While the conventional GO-PO/PTD methods are able to accurately calculate wedge contributions to scattered fields, the further propagation of diffracted rays is generally not considered in SBR approaches. Thus, the aim of this paper is to describe the implementation of diffracted rays according to the UTD concept into an SBR code. This novel implementation allows for the modeling of double diffraction and reflected-diffracted-reflected paths in complex scenarios consisting of a very large number of surface elements as well as the accurate simulation of cavities. The comparison with numerically exact reference simulations proves that the proposed hybrid GO/UTD-PO/PTD algorithm yields excellent results and that the UTD-SBR extension definitely improves the simulations of the ray tracing algorithm also for realistic objects.

Keywords: Numerical modeling, physical optics (PO), radar cross section (RCS), ray tracing, and uniform theory of diffraction (UTD).

I. INTRODUCTION

Accurate simulation of electromagnetic scattered fields is a very important research topic, because it is generally faster and cheaper than performing measurements, especially if complex or large-scale objects are involved. Moreover, a variety of geometry parameters can be studied easily and optimized, if required. Thus, the main application of such simulation programs is the prediction of scattered fields as well as the indication of scattering centers. The simulation results can be used to generate databases for target identification, for testing low-observability (LO) measures, and for developing specifications for various radar systems.

For finding the relevant propagation paths, most high-frequency approaches are using either a Shooting-and-Bouncing-Rays (SBR) algorithm [1, 2], which is commonly applied for objects made up of a very large number of surface elements, or the so-called image method (sometimes also referred to as image-tree method or method of images) [3-5], which works fine for a small number of large surface elements. In the context of high-frequency methods, sometimes a distinction is made between ray launching (in the sense of SBR) and ray tracing (in the sense of an image approach), which might lead to confusion. Generally, however, the term ray tracing is applied as umbrella term for all approaches using rays in order to find relevant propagation paths, i.e. SBR and image method are considered as different ray tracing approaches. The latter is also the convention used within this paper.

A very powerful ray tracing simulation approach based on SBR has been proposed in [1], showing excellent results even for complex objects such as real-scale aircraft at radar relevant frequencies. The algorithm is able to treat arbitrary objects and has practically no limitations concerning object size and the number of reflections to take into account. Due to the use of asymptotic methods, it is well-suited for simulations of large objects that cannot be modeled with numerically exact methods such as the Method of Moments (MoM) on current computer equipment. A detailed description of the algorithm as well as a discussion on alternative methods is available in [1].

This paper presents a further hybridization of the algorithm in order to improve the accuracy for lower frequencies, where diffraction is relevant. Although the approach in [1] considers diffracted field contributions within the Physical Theory of Diffraction (PTD) – which is similar to the XPATCH code [2] – the further propagation of diffracted rays is neglected, and so diffracted-reflected and double-diffracted ray paths, for example, are not included. However, these contributions may be significant at lower frequencies or at special geometries, as is proven in the following. After a brief review of the ray tracing algorithm presented in [1], which also demonstrates its limitations, the implementation of the Uniform Theory of Diffraction (UTD) is discussed in Section III. It must be pointed out that the aim of this paper is to describe the implementation of the UTD into an SBR code, rather than

explaining the details and limitations of the UTD itself. The simulation results in Section IV clearly show that the UTD extension provides a very useful enhancement of the ray tracing algorithm and definitely improves the accuracy of the results.

The UTD is a well-known high-frequency concept, which has been applied earlier within asymptotic methods, including hybrid SBR-image approaches [6] hybrid Finite-Elements methods [7], and mode matching approaches [8, 9]. However, combined reflected-diffracted propagation paths are not easy to treat in most UTD implementations, especially if higher-order interactions are relevant [4, 5, 10]. Contrary, the UTD implementation as presented in this paper avoids the analytical calculation of relevant diffracted propagation paths by following the SBR principles, i.e., starting from the point of diffraction, new rays are calculated and traced further through the scenario. This approach makes the UTD ray tracing algorithm much more versatile with the cost of increased computation efforts, of course. Nevertheless, today's development in fast computers makes the calculations executable on a standard PC with reasonable expenditure of time, so facetted CAD models of complex objects consisting of thousands or even hundreds of thousands of surface elements can be modeled with excellent accuracy.

II. RAY TRACING USING DISCRETE RAYS AND PO/PTD

A. Summary and Aim of the Implemented Ray Tracing Technique

This section will give a brief review on the implemented ray tracing approach, which is the basis for the UTD extension described in the subsequent sections. Emphasis will be put on the ray concept applied in the simulation code, rather than explaining the underlying theoretical principles. A more detailed description of the ray tracing algorithm and various simulation examples are available in [1]. The aim of this algorithm is to constitute a universally applicable high-frequency prediction tool, which can be used for RCS calculation of arbitrary complex objects by performing the simulation on facetted CAD models. For example, realistic aircraft models may require more than 100,000 facets with multiple interactions, which is the main reason why SBR is chosen in [1].

First of all, it must be noted that the implemented ray tracing algorithm works with discrete rays, which are taken as representatives of the so-called astigmatic ray tubes [11]. Thus, intersection tests with geometric structures are rather fast (compared to the tracing of ray tubes) on the one hand and on the other hand such a ray carries all necessary information of a ray tube, e.g. the radii of curvature of the corresponding wave front. Starting from a given transmitter, a specified number of rays is launched towards the object and traced according to the well-known SBR technique [12]. This approach allows the accurate modeling of large and complex objects because the required memory is independent of the number of reflections to take into account. The approach of discrete rays is combined with a ray-density normalization (RDN) [13], which provides the number of rays per cross section at any point of the ray trajectories.

However, the GO is not well-suited for calculating scattered fields of arbitrary finite objects because it assumes, e.g., reflections at infinitely extended surfaces. That is the reason why the RDN has been combined with Physical Optics (PO) and the PTD, which are able to calculate scattered fields as an integral over the surface and edges, respectively. As the RDN states the number of rays per unit area, it is used to calculate the equivalent surface area or edge length of each single ray hitting a geometrical object. This figure serves as the integration area for the PO and PTD formulation, respectively. However, it must be noted that the exact shape of the surface area corresponding to a single ray remains unknown. Fortunately, provided a dense grid of rays hits the surface (e.g. 10 rays per wavelength), the PO integral is proportional to the geometrical size of that area, so the surface area corresponding to a single ray can be assumed to be a square and the PO integral reduces to a sum of ray contributions.

In summary, the hybrid GO-PO/PTD approach uses the laws of GO (i.e. the law of reflection) merely for calculating geometrical ray propagation paths and the fields on these paths, while at each intersection of a ray with the object PO/PTD is applied for the scattered field contributions towards the point of observation.

B. Rays and Propagation Paths

For the understanding of the approach presented in this paper, it is important to distinguish between rays and propagation paths. In this context, a ray shall be defined as a directional straight geometrical connection between two points in three-dimensional space. Thus, e.g., a ray might hit a surface and generate a reflected ray, whose direction is given by the laws of GO. Additionally, the first ray generates a PO (or PTD) contribution to a point of observation, so the combination of the incident ray and the PO/PTD contribution shall be denoted as a propagation path. More generally speaking, a GO-PO/PTD propagation path consists of the incident ray (which hits the object), m reflected rays ($m \geq 0$), and one PO or PTD contribution to the point of observation. Thus, the approach of [1] accounts for single diffraction occurring at the last step of the propagation path. However, as is shown in this paper, diffracted rays are relevant for certain geometric objects. A diffracted ray is generated by a ray hitting an edge of the object, which means that the diffracted ray starts at the edge. In the further ray tracing process, this ray may also generate

reflected rays and PO/PTD contributions. Therefore a new class of propagation paths is introduced by the extension of the original approach: GO/UTD-PO/PTD propagation paths, which consist of the incident ray, m_1 reflected rays ($m_1 \geq 0$), one diffraction according to the laws of UTD, m_2 reflected rays ($m_2 \geq 1$), and finally one PO or PTD contribution to the point of observation. Note that $m_2 \geq 1$ is assumed because $m_2 = 0$ would result in calculating the contribution of diffracted fields to the point of observation, which is performed using PTD [1].

The GO/UTD-PO/PTD approach introduces paths with double diffraction but also other important single diffraction paths, which are generally not included in SBR codes. For example, an incident ray might hit the aperture edge of a cavity and generate diffracted rays propagating into the cavity. After m_2 reflections inside the cavity, a relevant contribution towards the receiver in the exterior space might be observed. As is shown in the following, these additional paths can significantly improve the accuracy of an SBR code, especially when cavities or general non-convex objects are involved.

C. Examples and Limitations of the GO-PO/PTD Approach

While the simulation examples in [1] show an excellent agreement of the ray tracing results with the reference data, this subsection emphasizes on special scenarios where diffracted rays might experience further interactions with the object and thus yield significant contributions that are neglected in the GO-PO/PTD approach.

A classic reference object is the trihedral corner reflector (e.g., [5, 14]), which is made up of three right-angled triangles that are assembled like a pyramid. Here, the object has an edge length of $a = 1.41$ m at the aperture. The aperture angle is $\gamma = 90°$ and the Trihedral is inclined by $\alpha_0 = 35,3°$ in the direction of elevation (see Fig. **1**). Thus, the x-axis is perpendicular to the aperture. The faces of the Trihedral are assumed to have zero thickness.

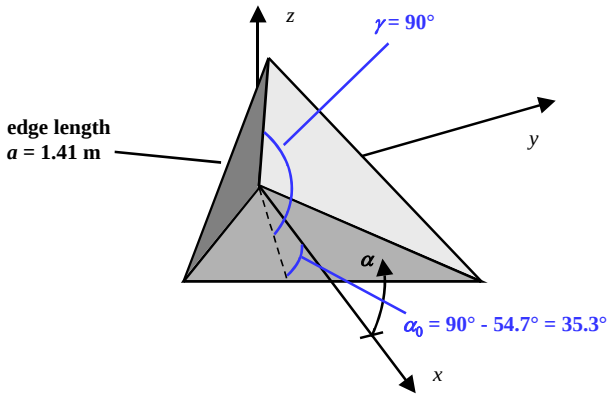

Fig. 1. Geometry of the trihedral corner reflector.

As can be seen in the monostatic RCS simulations in [1], the PTD provides a significant improvement compared to the PO only simulation (note that [1] uses $\alpha' = -\alpha$). However, deviations are observed at angles where the observation point is close to the aperture plane, i.e. $\alpha \rightarrow \pm 90°$. As will be shown later, these deviations are due to missing diffracted field contributions. An even more severe deviation is found in the results of the bistatic RCS simulation of the Trihedral. An example simulation has been performed depending on the elevation angle α with a total of $N = 10$ million rays (Fig. 2). The direction of the incident wave is perpendicular to the aperture, i.e., $\alpha_i = 0°$. As can be seen from the reference Boundary-Integral-MLFMM (BI-MLFMM) simulation, the RCS curve of the vv-polarization exhibits a distinct step around $\alpha = -35°$, which is not reproduced at all with the ray tracing simulation results. Furthermore, both polarizations show major deviations in the angular range from +90° to +145°, which is part of the forward-scattering halfspace. For a better understanding of these results, a detailed analysis of the corresponding scattering directions and the relevant propagation paths is necessary. Obviously, the maximum of the bistatic RCS corresponds to the backscattering case, whereas the second maximum at $\alpha = -70°$ is caused by rays hitting the Trihedral near the top corner (see Fig. 1). Due to geometrical reasons, the corners do not contribute to triple reflection [15]. Thus, such rays are doubly-reflected in that corner and – instead of a third reflection at the lower facet – exit the scenario towards the angle $\alpha = -70.6°$. From these considerations, the step at $\alpha = -35°$ can be interpreted as a shadow effect caused by the lower facet. From $\alpha = 0°$ to $\alpha = -35°$, the complete interior of the Trihedral is visible to the observation point, so no shadowing effects will occur. Contrary, the interior of the lower facet is not visible at angles beyond -35°. A similar effect is observed at angles beyond +90°. Here the interior of the Trihedral is not visible at all, which leads to rather small RCS values. In this angular region, diffraction at the aperture wedges is the main propagation mechanism. Note that the maximum at $\alpha = \pm 180°$ corresponds to forward scattering and does not represent the total field strength.

According to the ray tracing method described in [1], each reflection of a GO ray is associated with a PO (and possibly PTD) surface current, which yields a contribution to the scattered field strength. Thus, shadowing effects are reproduced by the superposition of at least two PO contributions. As an example, consider an incident ray hitting the lower facet. In the basic form of the algorithm, the PO surface current contribution is calculated to any observation point, regardless of visibility. The reflected ray hits one of the upper facets and generates a second PO surface current. Ideally, these contributions should interfere destructively for

observation points that are not visible from the point of the first reflection. However, this is true only for observation points located in the specular direction of the first reflection (at $\alpha = 110°$). That is the reason why the results are closer to the reference solution at this angle (see Fig. 2). For observation points within the angular range from +90° to +145° but deviating from the specular direction, the phases of the two contributions are no longer correct, which results in the major inaccuracies observed in Fig. 2. At angles beyond +145°, the observation points are located behind the plane containing the lower facet, so forward scattering is the main contribution and yields a good accuracy.

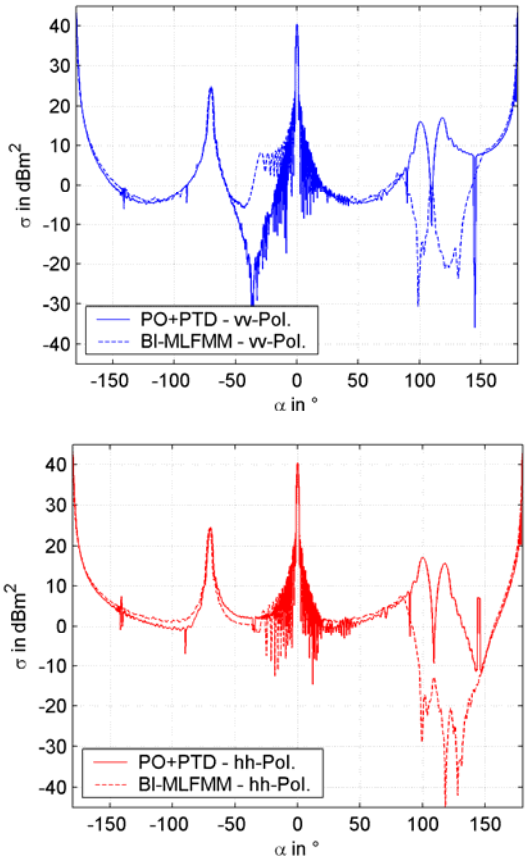

Fig. 2. Bistatic RCS of the trihedral corner reflector ($f = 15$ GHz, PO/PTD without shadowing).

As a possible improvement to the shadowing problem, in Fig. 3 contributions are calculated only if the observation point is visible from the point of interaction and, additionally, for forward scattering. The result of this approach shows definitely improved data in the range from +90° to +145°. But, unfortunately, the results are worse in other angular regions, especially for the vv-polarization at angles beyond -70°. Note that small peaks, e.g. at $\alpha = +145°$, are due to the fact that the implemented PTD shows a singularity at grazing angles. Thus, these observation points are excluded from the PTD calculation, leading to a distinct step in the RCS curve. To summarize these studies, the example of bistatic scattering from a trihedral corner reflector clearly shows that the GO-PO/PTD approach has definite limitations at certain geometrical structures.

Another important example of more practical use is a cavity, e.g. as described in [12]. Cavities are often used as simple models of jet engine inlet ducts, which are rather complex objects in the view of electromagnetic (EM) modeling. Thus, a variety of approaches has been studied in order to accurately model these objects, e.g. modal methods, GO with Aperture Integration, Gaussian Beams, Finite Element methods, and Iterative Physical Optics (IPO) [12, 16, 17, 18].

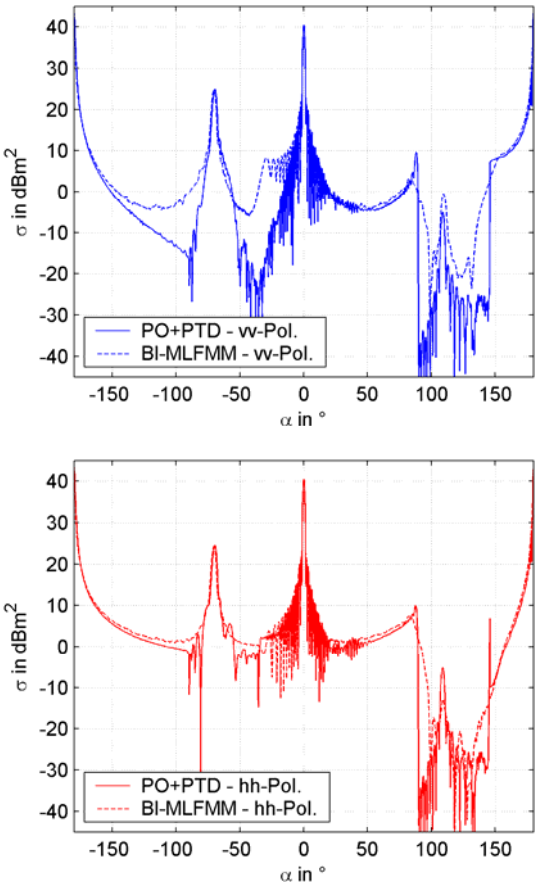

Fig. 3. Bistatic RCS of the trihedral corner reflector ($f = 15$ GHz, PO/PTD with shadowing).

The object of the following studies consists of a cubic cavity with a side length of 10 λ ($f = 3$ GHz) and is a very elementary step towards the modeling of engine ducts. Additionally, this object is surrounded by a wall of 1 λ thickness. The simulated monostatic RCS of the cavity is given in Fig. 4, together with the result of the

reference BI-MLFMM simulation. The angle α denotes the elevation angle with respect to the axis of the cavity, i.e., $\alpha = 0°$ corresponds to the incidence perpendicular to the aperture.

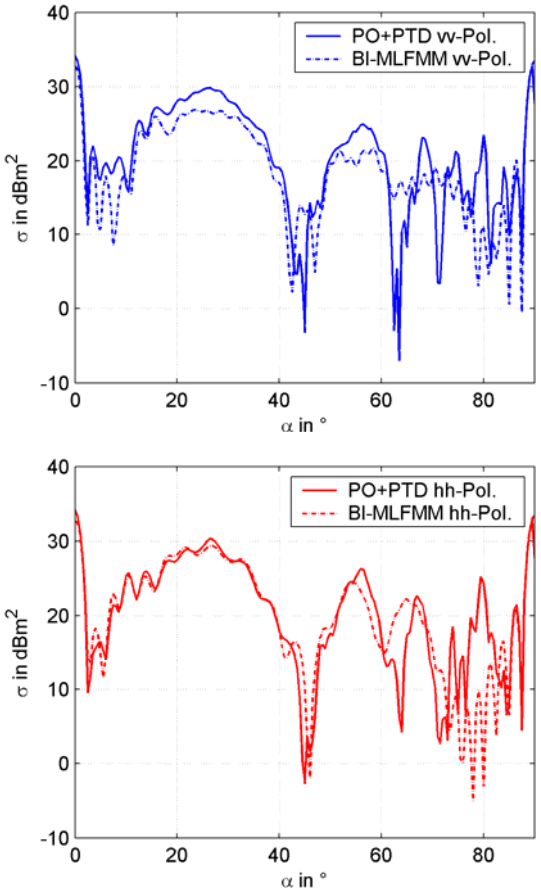

Fig. 4. Monostatic RCS of the cubic cavity ($f = 3$ GHz, $l = 10\ \lambda$, PO/PTD).

A longer cavity ($l = 30\ \lambda$) has also been modeled (see results in Fig. 5). Apart from the surrounding wall of 1 λ thickness, this object is identical to one of the simulation examples in [12]. As becomes obvious from Figs. 4 and 5, the GO-PO/PTD ray tracing algorithm basically provides a satisfying accuracy at most angles. However, major deviations can be found at large elevation angles, which partly originate from the almost grazing incidence of rays at the aperture. Thus, the rays experience a large number of reflections inside the cavity, which is accounted for by setting the maximum number of reflections to $R_{max} = 50$. Simulations with a higher number of reflections showed that this value is enough to ensure convergence. Thus, the deviations may be due to coupling effects that are not covered by the ray tracing approach.

A closer look at the cavities and the trihedral corner reflector reveals that a complete class of possibly relevant propagation paths has been neglected so far, because the ray tracing algorithm presented in [1] does not trace diffracted rays. However, a ray may be diffracted at the aperture, continue propagating into the cavity, and finally – when it exits from the cavity – provide a significant contribution to the scattered field. In order to accomplish the tracing of diffracted rays, the implementation of the Uniform Theory of Diffraction (UTD) into the algorithm presented in [1] is described in the following section. Concerning the ray tracing procedure, the UTD for diffracted rays is the counterpart to the GO for reflected rays. It is important to note that in the simulation approach presented in this paper, the geometrical propagation paths and the fields on these paths are calculated according to the laws of GO and UTD (i.e. the law of reflection and the law of edge diffraction on the Keller cone), while the field contributions towards the point of observation are determined by PO and PTD, respectively. Thus, each time a ray hits a surface or edge, a PO (and possibly also PTD) current is calculated, which generates a contribution to the total scattered field strength. Altogether, a hybrid GO/UTD-PO/PTD simulation approach is developed.

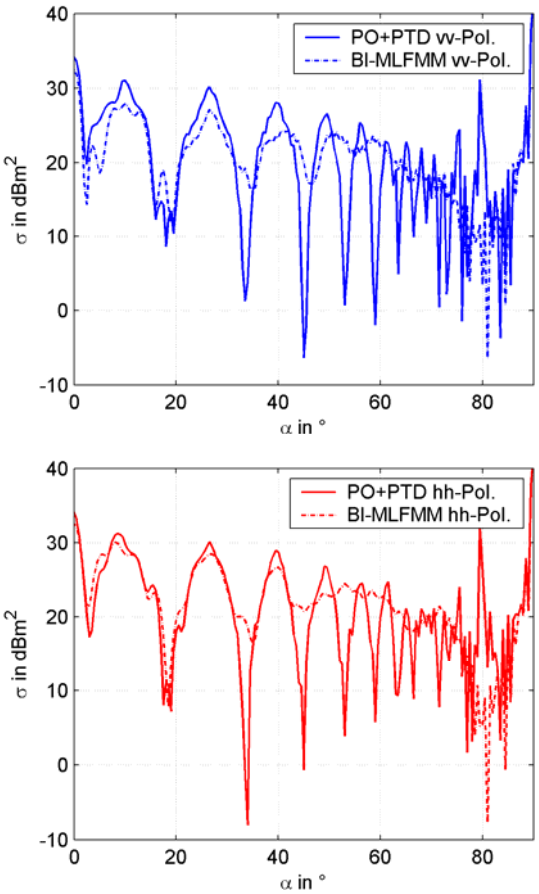

Fig. 5. Monostatic RCS of the cuboid cavity ($f = 3$ GHz, $l = 30\ \lambda$, PO/PTD).

III. THE UNIFORM THEORY OF DIFFRACTION

A. Principles of the UTD

The UTD is a well-known high-frequency technique for the asymptotic calculation of diffracted fields and has been studied in various publications. In the present paper, only the basic UTD approach of diffraction from an infinite perfectly conducting wedge will be applied [19] in order to keep the additionally required CPU efforts as small as possible. Thus, there is no special treatment of shadow boundaries and no distinction between near and far field [3]. There are also UTD approaches for impedance edges [21, 22], which, of course, are much more complex than the standard UTD formulation.

Concerning the implementation in a ray tracing algorithm, the most important attribute of the UTD concept is the assumed limitation of the diffracted field to the so-called Keller cone [20], which is the equivalent to the specular reflection of the GO. Each propagation path on the Keller cone can be identified with an angle ϕ, $0° < \phi < n\pi$, where $n\pi$ is the outer wedge angle. The angle β between the diffracted ray and the edge is identical to the angle β' between the incident ray and the edge. In the present form, UTD diffraction is applied only for first order diffraction. However, second order diffraction is implied by performing PTD on diffracted rays if they hit another edge.

The UTD diffracted fields are basically determined by diffraction coefficients D_s and D_h (soft and hard polarization), which – similarly to the Fresnel reflection coefficients – denote the ratio between the incident field strength E^i and the diffracted field strength E^d,

$$E^d(s) = D_{s,h} A(s) E^i \tag{1}$$

s denotes the distance from the edge to the point of observation [19]. $A(s)$ is the spread factor describing the divergence of the diffracted wave and the D_s and D_h depend on the angle of incidence, the wedge angle, frequency, etc., and in a secondary way also on the distance s. In the context of the present paper, s does not correspond to a real far field point of observation, but is equal to the distance to the next intersection point on the object. From the view of the ray tracing algorithm, the quantity s is unknown at the time of calculating the diffraction coefficients because, typical to a SBR-algorithm, no information on the future propagation path is available. Fortunately, this problem can be solved rather easily by launching a dummy ray to determine the distance to the next intersection or by applying the UTD coefficients later when s is known.

Of course, due to the assumed simplifications, inaccuracies might occur if the next intersection point is too far away from an edge with finite length. Nevertheless, the results in Section IV show good accuracy for all simulation examples.

B. Application to the Ray Tracing Technique

According to the electromagnetic problem to be solved, different implementations of the theoretical concept of the UTD are known in literature. For example, if the problem consists of large flat surface elements, an image approach of UTD is rather convenient [6, 7]. For resonant structures such as large open-ended waveguides, a modal approach has been developed, which converts UTD diffracted rays into modes [8, 9]. This paper proposes a novel implementation of the UTD in a ray tracing code using discrete rays and RDN. Thus, the UTD is implemented in a pure SBR fashion, which is consistent to the original ray tracing code as summarized in Section II.

Consider a ray that hits a wedge within the simulation scenario. According to the description in [1], this ray generates a PO contribution as well as a PTD contribution and afterwards is reflected towards the specular direction. Additionally, the UTD diffraction has to be performed, but at this stage, the relevant propagation paths are unknown. Note that a diffracted ray may experience several reflections before it generates a significant PO/PTD contribution towards an observation point. That is the reason why in the approach presented in this paper a large number N_{UTD} of rays is generated on the Keller cone and further traced through the scenario according to the SBR principles. Like the original ray, the diffracted rays will generate PO and PTD contributions each time they hit a surface or edge. Theoretically, even higher order UTD diffraction can be treated with this approach, provided that shadow boundaries are treated adequately, but in most practical cases, such effects will not provide a relevant contribution to the total scattered fields. Actually, double diffraction is considered implicitly by using PTD for the second diffraction.

As at the stage of diffraction the directions of relevant propagation paths are unknown, it is most convenient to uniformly distribute the diffracted rays on the Keller cone. Thus, each diffracted ray is defined by assigning an angle $\phi_k = (k\text{-}0.5)n\pi/N_{\mathrm{UTD}}$, $k = 1,\ldots, N_{\mathrm{UTD}}$. This means that the Keller cone is cut into N_{UTD} parts, and one ray is launched in the center of each part. This definition is implemented in the ray tracing algorithm, with an additional stochastic variation of the angles ϕ_k, so that in each part of the Keller cone a diffracted ray is launched at a random angle $(k\text{-}1)n\pi/N_{\mathrm{UTD}} < \phi_k < k\, n\pi/N_{\mathrm{UTD}}$, $k = 1,\ldots, N_{\mathrm{UTD}}$. As stated in [1], such a variation reduces aliasing effects, which might occur, for example, at the edges of plane facets.

While these considerations are more or less obvious, the remaining problem is more complicated. As the presented ray tracing algorithm works with the RDN, which weights each contribution according to the ray

density, the correct density of the diffracted rays has to be determined. Generally, the ray density n_d states the number of rays per unit area perpendicular to the direction of propagation. In the context of PO and PTD it is needed to calculate the equivalent surface area and edge length, respectively, of a ray hitting the object.

To clarify the problem, a two-dimensional configuration is considered first (Fig. 6). The object is represented by a half-plane, which is hit by an incident plane wave at the angle β. This scenario corresponds to a cut for a fixed diffraction angle ϕ. Note that in this specific 2D-case the "diffracted" rays have the same direction like the reflected rays, and the Keller cone reduces to a straight line, which means each incident ray will generate one diffracted ray towards the specular direction. According to the definition of the ray density, the distance between adjacent rays in the 2D-case is $1/n_d$. Thus, each ray can be assigned an equivalent edge length,

$$dl = \frac{1}{n_d \sin\beta} . \tag{2}$$

The distance between adjacent diffracted rays is,

$$\frac{1}{n_d'} = dl \sin\beta = \frac{1}{n_d} . \tag{3}$$

As expected, the ray density n_d' of the diffracted wave is equal to the ray density of the incident wave. This statement is also true if the incident rays are divergent. In that case, both n_d and n_d' contain a divergence factor, which depends on the path length. Nevertheless, equation (3) is still valid with these considerations.

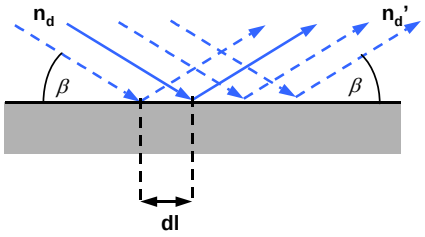

Fig. 6. Two-dimensional diffraction scheme for calculating the ray density.

The realistic case, however, is a three-dimensional scenario with incident rays being diffracted at an edge (outer wedge angle $n\pi$) of the object. Similar to the 2D-case, the incident ray density is denoted as n_d, but here the equivalent cross section of a ray is equal to $1/n_d$. Each ray that hits the edge generates a Keller cone of N_{UTD} diffracted rays, as described above. To calculate the ray density of the diffracted rays, the equivalent cross section of the diffracted rays, $1/n_d'$, has to be determined. Apparently, this equivalent cross section is equal to the distance between adjacent rays on one Keller cone (U / N_{UTD}) multiplied by the distance between adjacent Keller cones ($dl \sin\beta$), i.e.,

$$\frac{1}{n_d'} = \frac{U}{N_{\mathrm{UTD}}} dl \sin\beta , \tag{4}$$

where U denotes the perimeter of the Keller cone,

$$U = \frac{n\pi}{2\pi} 2\pi s \sin\beta . \tag{5}$$

In equation (5), s denotes the distance from the point of diffraction to the point of observation, which is equivalent to the next intersection point of the ray with the object. As a result, the ray density of the diffracted rays is calculated according to,

$$n_d' = N_{\mathrm{UTD}} \frac{1}{n\pi \sin^2\beta dl\, s} . \tag{6}$$

The equivalent edge length, dl, depends on the incident ray density n_d and the edge width relevant for diffraction [1]. Equation (6) provides the relationship for the correct weighting of UTD diffracted field contributions and is valid even if the incident wave is not a plane wave. In that case, a possible divergence, for example, is included in the incident ray density n_d and thus in the equivalent edge length dl [1].

The following section shows that the described implementation of the UTD into the SBR algorithm allows for a definite improvement of simulation results, especially for resonant structures. All simulations consider a maximum of one UTD diffraction on each propagation path, which might be followed by an additional PTD diffraction, so doubly-diffracted field contributions are included.

IV. GO/UTD-PO/PTD SIMULATION RESULTS

A. Trihedral and Cavities with UTD

In this section the simulation examples of Section II are modeled with the additional consideration of UTD diffracted rays. Figure 7 shows the UTD results of the trihedral corner reflector as described in Fig. 1. Obviously, the simulation results are definitely improved in comparison to Figs. 2 and 3. Especially the step in the curve for the vv-polarization around the angle α = -35° is reproduced almost exactly. Besides, the characteristic resonances in the angular range from -30° to +20° are exactly at the same angles like in the reference BI-MLFMM simulation. Apart from these excellent

agreements, Fig. 7 also shows a better accuracy than Fig. 2 in the angular range from +90° to +145°. The small peak in the curve of the hh-polarized RCS at $\alpha = 145°$ corresponds to the exclusion of PTD calculation at grazing angles, which has been discussed in Section II. Note that shadowing effects are not explicitly considered in Fig. 7.

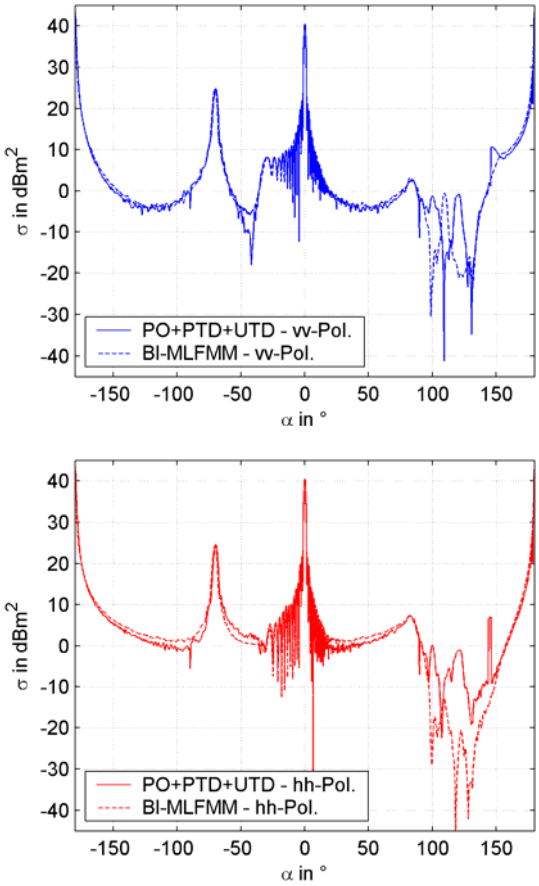

Fig. 7. Bistatic RCS of the trihedral corner reflector ($f = 15$ GHz, $N_{UTD} = 1{,}000$).

Altogether, it is apparent that the UTD provides a relevant contribution to the scattered field in the example of the trihedral corner reflector. Rays hitting the edges of the trihedral are diffracted and have at least one more reflection at the object. As can be deduced from Fig. 7, only the tracing of such propagation paths will provide accurate results over almost the complete angular range of the bistatic RCS.

However, the drawback of this UTD implementation is the increased CPU time for the simulation. The reason for this is the need for a fine scanning of the object, i.e. the number of diffracted rays must be "large enough". The precise meaning of this expression depends on the object, of course, but the value $N_{UTD} = 1000$ proved good results in all examples studied so far. The simulation of Fig. 7 has also been performed with $N_{UTD} = 100$ and $N_{UTD} = 10$ (see Section IV.B), which leads to basically the same results but the curves are less smooth. When using UTD-SBR with a very large number of diffracted rays ($N_{UTD} = 10{,}000$, see Table 1), a tremendous increase of CPU time is observed, while no further improvement of results is possible because the data show convergence with respect to the number of diffracted rays.

Table 1. CPU times for numbers of UTD rays (on Athlon XP3000+ processor).

Simulation parameters	CPU time
$N = 10$ million, without UTD	20 h
$N = 10$ million, $N_{UTD} = 10$	21 h
$N = 10$ million, $N_{UTD} = 100$	23 h
$N = 10$ million, $N_{UTD} = 1{,}000$	40 h
$N = 10$ million, $N_{UTD} = 10{,}000$	262 h

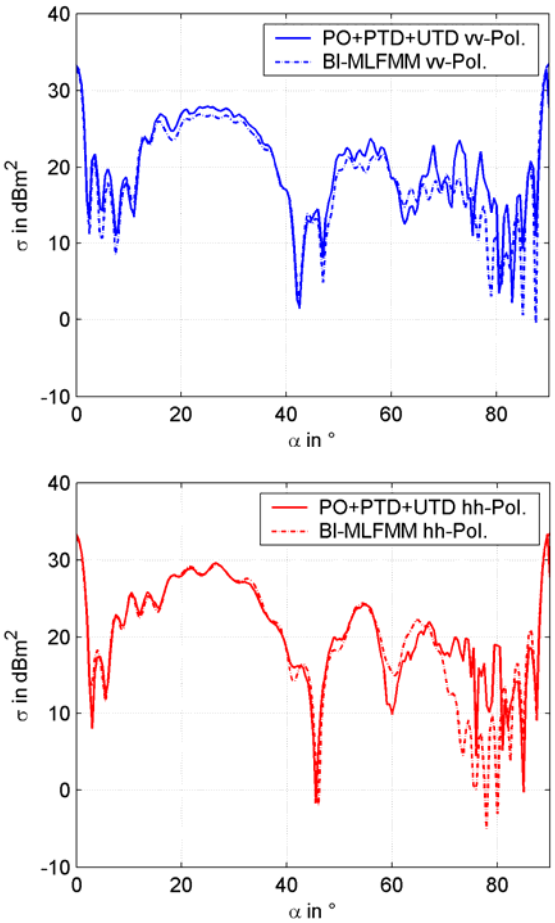

Fig. 8. Monostatic RCS of the cubic cavity ($f = 3$ GHz, $N_{UTD} = 1{,}000$).

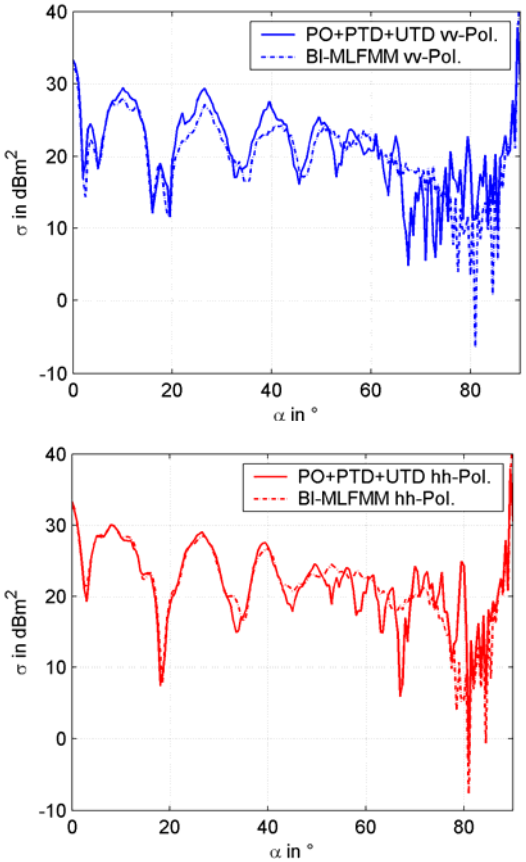

Fig. 9. Monostatic RCS of the cuboid cavity (f = 3 GHz, N_{UTD} = 1,000).

As can be deduced from Table 1, the CPU time for the calculation without UTD is around 20 h, which appears rather high for this simple object. The main reason for the stated CPU time is the angular resolution of the bistatic RCS, $\Delta\alpha = 0.25°$, which means that at each intersection of a ray with the object, PO and/or PTD contributions have to be calculated to 1,441 observation points. As the algorithm is not yet optimized for such a large number of receivers, the time for the PO/PTD calculations is much larger than the CPU time for the geometrical ray tracing, i.e. the calculation of propagation paths.

If UTD is considered with N_{UTD} = 100, the CPU time is increased only by 15%. In contrast, the CPU time is more than doubled with N_{UTD} = 1,000, and it increases by a factor 13 if N_{UTD} is set to 10,000. However, no significant improvement is observed at N_{UTD} = 10,000. From Table 1 it is obvious that at N_{UTD} = 1,000, more than half of the CPU time is spent with the calculation of UTD diffracted rays and the associated PO/PTD contributions. The convergence of results depending on the number of diffracted rays N_{UTD} is considered more in detail in Section IV.B.

For practical use, the example of the cavities studied in Section II.C is more important. Consider a ray that hits the object at one edge of the aperture. According to the method described in the previous section, this ray generates N_{UTD} diffracted rays, of which approx. one third will enter the cavity. Note that the outer wedge angle is $3\pi/2$, and only the angular range $\phi = 0$ to $\phi = \pi/2$ (measured from the inner walls) will lead to rays propagating into the cavity. These rays are further traced according to the SBR technique and provide additional contributions which are not included in the original PO/PTD version of the algorithm. The results of the simulations are shown in Figs. 8 and 9, which present an excellent improvement of the RCS data with respect to the reference MoM simulation, especially in the angular range from 0° to 60°. It is remarkable that in this range the RCS for hh-polarization is practically identical to the reference, while the RCS for vv-polarization is slightly higher than the results of the MoM simulation.

B. Convergence and Low-Frequency Considerations

As stated above, the simulation results in Section IV.A have been obtained by generating 1,000 diffracted rays for each ray hitting an edge of the object, i.e. N_{UTD} = 1,000. This setting proved to yield satisfying results but leads to the significant drawback of more than double CPU time in the case of the trihedral corner reflector. Thus, it is very important to study the convergence of the results when using the UTD extension at different values for N_{UTD}.

For this purpose, the simulation shown in Fig. 7 has been repeated at N_{UTD} = 10 and N_{UTD} = 100 (Figs. 10 and 11 – for convenience, only the results for vv-polarization are given in this paper). As becomes obvious from Fig. 10, the setting N_{UTD} = 10 already leads to the correct shape of the bistatic RCS curve, including the step at the angle α = -35°. However, the curve is overlaid by smaller fluctuations, which are caused by the stochastic nature of the described approach. Nevertheless, the relatively small number of diffracted rays provides good results in this test case, while only a small amount of additional CPU time is required.

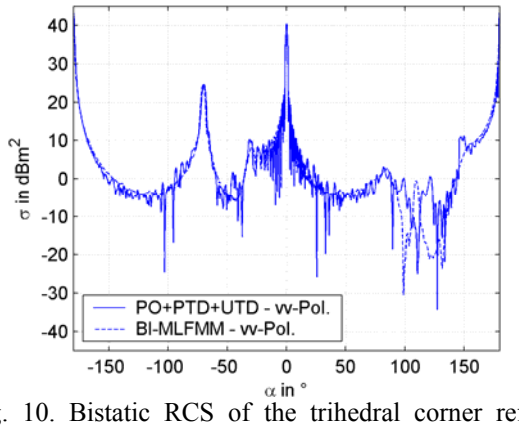

Fig. 10. Bistatic RCS of the trihedral corner reflector (f = 15 GHz, N_{UTD} = 10).

As can be expected from the law of large numbers, the fluctuations decrease at $N_{UTD} = 100$ (Fig. 11), but for high-quality results, $N_{UTD} = 1{,}000$ should be chosen (cf. results in Fig. 7). Also, it must be noted that the required number of diffracted rays is always connected to the number N of rays in the simulation. For example, if $N' = 10\,N$ is used in a second simulation, the number N_{UTD} of diffracted rays on a single Keller cone can be decreased to one tenth of the original value, in order to obtain the same density of diffracted rays and thus the same accuracy of the UTD diffracted rays contribution.

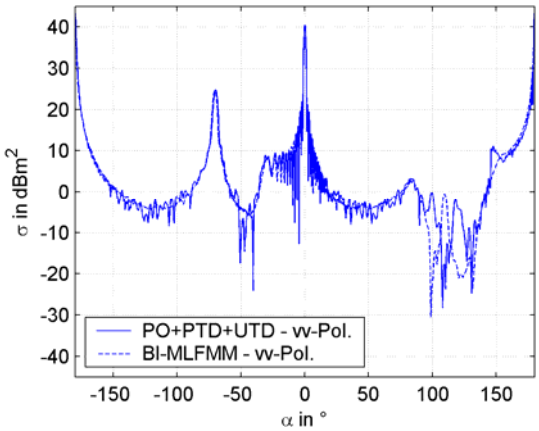

Fig. 11. Bistatic RCS of the trihedral corner reflector ($f = 15$ GHz, $N_{UTD} = 100$).

Further studies have been made with respect to the frequency range, in which the presented UTD implementation is valid. It is well-known that the UTD as implemented in the ray tracing algorithm assumes infinitely extended edges. That is the reason why this method is a typical asymptotic or high-frequency approximation. In the test case studied above ($f =$ 15 GHz) the length of the wedges at the aperture is 50 wavelengths. The same object has also been studied at $f = 6.4$ GHz and $f = 3$ GHz, where the relative wedge lengths are 21 wavelengths and 10 wavelengths, respectively. As can be deduced from Figs. 12 and 13, the UTD extension still works very well at both frequencies. Especially the step of the curve at $\alpha =$ -35°, which is independent of frequency, is reproduced almost exactly. Although there are some minor oscillation artefacts at 3 GHz, the accuracy of the GO/UTD-PO/PTD algorithm is remarkable.

It must be pointed out that the UTD simulations in this section have been performed by considering a maximum of one UTD diffraction for each ray. Thus, doubly diffracted paths (first UTD, later PTD, possible reflections before UTD or between UTD and PTD) are included. Further simulations at $f = 3$ GHz have been studied by considering a maximum of two and three UTD diffractions for each ray. These settings lead to an immense increase of CPU time but – apart from additional "clutter" – do not provide a significant change of simulation results. Consequently, double UTD diffraction does not yield a relevant contribution in this example, as might have been expected. Thus, the simulations in this section can be regarded to be convergent not only with respect to the number N_{UTD} of diffracted rays on the Keller cone, but also in terms of multiple diffractions.

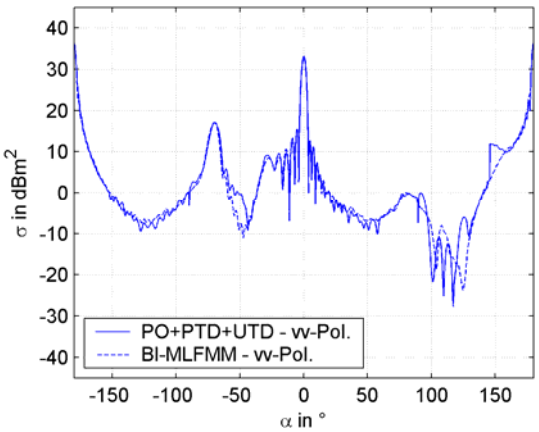

Fig. 12. Bistatic RCS of the trihedral corner reflector ($f = 6.4$ GHz, $N_{UTD} = 1000$).

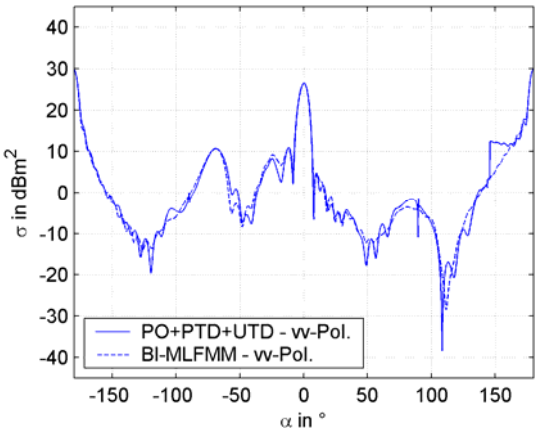

Fig. 13. Bistatic RCS of the trihedral corner reflector ($f = 3$ GHz, $N_{UTD} = 1000$).

C. Generic Missile Model

The last simulation example is a generic missile model consisting of 44,000 triangular facets, which has been proposed in [23]. A picture of the CAD model can be found in [1], where the monostatic RCS has been calculated in the azimuth plane for vv-polarization at $f = 12$ GHz. This simulation is repeated here with the additional consideration of UTD contributions as described above. Although the results in Fig. 14 suggest an even better agreement than without UTD, the mean error of both simulations is exactly the same (1.7 dB). However, if only the angular range from $\phi = 140°$ to

$\phi = 180°$ is considered, i.e. the angles with the most distinct deviation in [1], the mean error decreases from 2.5 dB without UTD to 2.2 dB with the use of UTD. Thus, the UTD improves the results for angles, where the wave impinges on the wedged back side of the wings, whereas a slight stochastic deviation is imposed at angles with excellent agreement compared to the reference data. Using $N_{UTD} = 1{,}000$ for this simulation, the CPU time is increased by approx. 16%, which is an acceptable effort for this object. Thus, this simulation example proves that the application of the implemented UTD is practicable not only for simple objects but also for realistic CAD models.

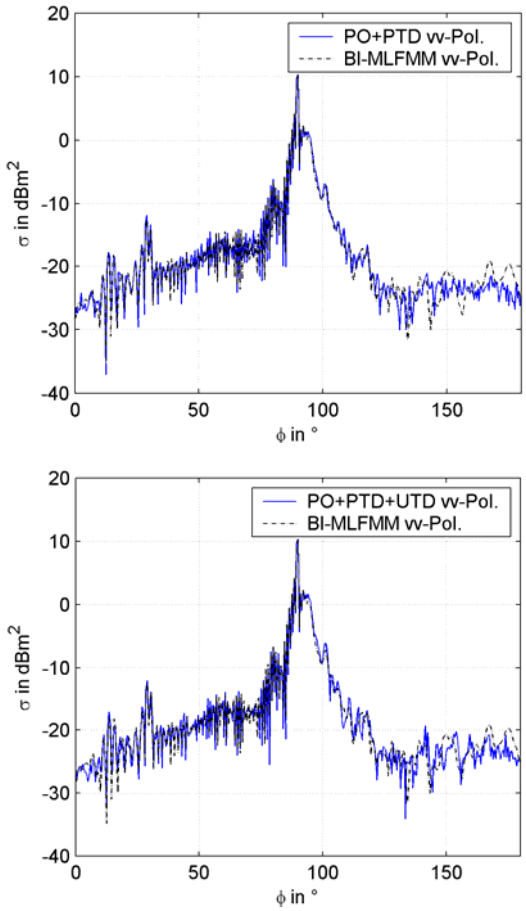

Fig. 14. Monostatic RCS of the generic missile at $f = 12$ GHz, vv-polarization.

The generic missile has also been studied in terms of bistatic RCS. The incident wave is parallel to the *xy*-plane and hits the object at $\phi_0 = 135°$, i.e. from the rear side (Fig. 15). For the evaluation of results, the bistatic angle ϕ is calculated from the nose direction. Specular reflection from the body of the missile is expected at $\phi = 45°$, forward scattering is equivalent to $\phi = 315°$. As in the previous simulation, the frequency is 12 GHz and the vv-polarized fields are evaluated.

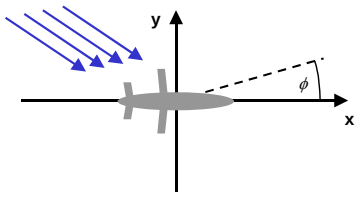

Fig. 15. Geometric scheme for bistatic RCS simulations of the generic missile.

From the results in Fig. 16, it can be observed that the original GO-PO/PTD algorithm already yields rather accurate results. However, as the dynamic range is very large, significant deviations occur at certain angles, leading to a mean error of 8.6 dB. By tracing UTD diffracted rays, this error is reduced to 7.9 dB. Obviously, additional propagation effects and coupling mechanisms, such as creeping waves, are relevant when studying bistatic RCS of a convex-like target. Nevertheless, the accuracy of the bistatic results obtained by the presented ray tracing algorithm is remarkable, both for the original GO-PO/PTD version as well as for the newly developed UTD Shooting-and-Bouncing extension.

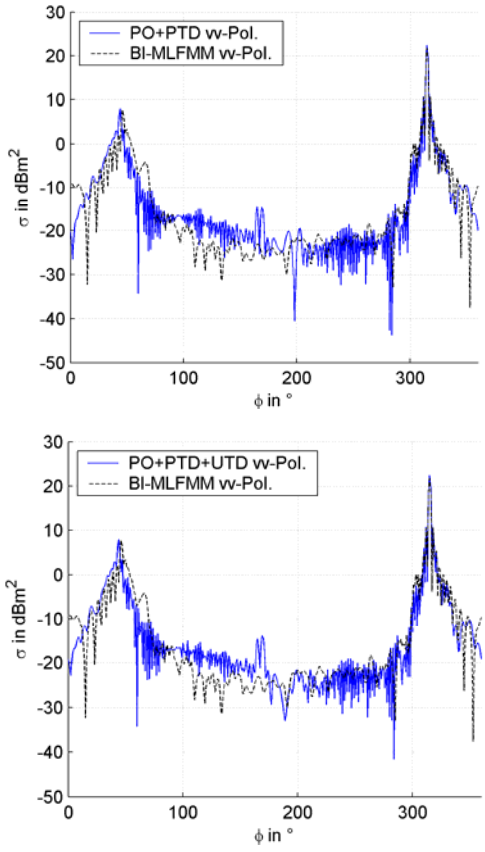

Fig. 16. Bistatic RCS of the generic missile at $f = 12$ GHz, vv-polarization.

V. CONCLUSION

This paper presents an important extension to the formerly proposed GO-PO/PTD ray tracing algorithm for RCS simulations of large and complex objects. The novel implementation of the UTD in a SBR fashion makes each relevant ray generate a given number of diffracted rays on the Keller cone, which are further traced through the scenario. Thus, reflected-diffracted-reflected propagation paths with multiple reflections and one diffraction in between are added to the original SBR concept. The combination of the well-known UTD and the newly developed, sophistiacted adaptation of the ray-density normalization to diffracted rays provides a very powerful algorithm to analyze the scattered fields of arbitrary objects. While the original GO-PO/PTD formulation provides excellent results at more or less convex objects, the UTD extension is required where diffracted rays might experience further interactions with the object and thus generate relevant contributions to the total scattered fields. A typical example for that case is a cavity, where rays are diffracted at the aperture and subsequently propagate into the cavity. However, also complex realistic objects can be treated by the hybrid GO/UTD-PO/PTD algorithm. As is shown by comparison with numerically exact solutions in the examples above, the elementary implementation of the UTD extension already provides very accurate results for both canonic and realistic objects.

REFERENCES

[1] F. Weinmann, "Ray tracing with PO/PTD for RCS modeling of large complex objects," *IEEE Trans. Antennas Propagat.*, vol. 54, pp. 1797-1806, June 2006.

[2] D. J. Andersh, M. Hazlett, S. W. Lee, D. D. Reeves, D. P. Sullivan, and Y. Chu, "XPATCH: A high frequency electromagnetic-scattering prediction code and environment for complex 3d objects," *IEEE Antennas and Propagation Magazine*, vol. 36, pp. 65-69, Feb. 1994.

[3] W. D. Burnside and R. J. Marhefka, "Antennas on Aircraft, Ships, or Any Large, Complex Environment," Chapter 20 in *Antenna Handbook Volume III, Applications*, edited by Y. T. Lo and S. W. Lee, Van Nostrand Reinhold, New York, 1993.

[4] E. H. Newman and R. J. Marhefka, "Overview of MM and UTD methods at the ohio state university," *Proc. IEEE*, vol. 77, pp. 700-708, May 1989.

[5] A. C. Polycarpou, C. A. Balanis, and C. R. Birtcher, "Radar cross section of trihedral corner reflectors: theory and experiment," *Electromagnetics*, vol. 15, no. 5, pp. 457-484, Sept.-Oct. 1995.

[6] S.-H. Chen and S.-K. Jeng, "An SBR-image approach for radio wave propagation in indoor environments with metallic furniture," *IEEE Trans. Antennas Propagat.*, vol. 45, pp. 98-106, Jan. 1997.

[7] A. Tzoulis and T. F. Eibert, "A hybrid FEBI-MLFMM-UTD method for numerical solutions of electromagnetic problems including arbitrarily shaped and electrically large objects," *IEEE Trans. Antennas Propagat.*, vol. 53, pp. 3358-3366, Oct. 2005.

[8] A. Altintas, P. H. Pathak, and M.-C. Liang, "A selective modal scheme for the analysis of EM coupling into or radiation from large open-ended waveguides," *IEEE Trans. Antennas Propagat.*, vol. 36, pp. 84-96, Jan. 1988.

[9] P. H. Pathak and A. Altintas, "An efficient high-frequency analysis of modal reflection and transmission coefficients for a class of waveguide discontinuities," *Radio Science*, vol. 23, pp. 1107-1119, Nov.-Dec. 1988.

[10] T. Griesser and C. A. Balanis, "Backscatter analysis of dihedral corner reflectors using physical optics and the physical theory of diffraction," *IEEE Trans. Antennas Propagat.*, vol. 35, pp. 1137-1147, Oct. 1987.

[11] C. A. Balanis, *Advanced Engineering Electromagnetics*, New York: John Wiley & Sons Inc., 1989.

[12] H. Ling, R.-C. Chou, and S.-W. Lee; "Shooting and bouncing rays: Calculating the RCS of an arbitrarily shaped cavity," *IEEE Trans. Antennas Propagat.*, vol. 37, pp. 194-205, Feb. 1989.

[13] D. Didascalou, T. M. Schäfer, F. Weinmann, and W. Wiesbeck, "Ray-Density normalization for ray-optical wave propagation modeling in arbitrarily shaped tunnels," *IEEE Trans. Antennas Propagat.*, vol. 48, pp. 1316-1325, Sep. 2000.

[14] J. Baldauf, S.-W. Lee, L. Lin, S.-K. Jeng, S. M. Scarborough, and C. L. Yu, "High frequency scattering from trihedral corner reflectors and other benchmark targets: SBR versus experiment," *IEEE Trans. Antennas Propagat.*, vol. 39, pp. 1345-1351, Sep. 1991.

[15] E. F. Knott, J. F. Shaeffer, and M. T. Tuley, *Radar Cross Section – Second Edition*, Norwood: Artech House Inc., 1993.

[16] P. H. Pathak and R. J. Burkholder, "Modal, ray, and beam techniques for analyzing the EM scattering by open-ended waveguide cavities," *IEEE Trans. Antennas Propagat.*, vol. 37, pp. 635-647, May 1989.

[17] H. T. Anastassiu, J. L. Volakis, D. C. Ross, and D. Andersh, "Electromagnetic scattering from simple jet engine models," *IEEE Trans. Antennas Propagat.*, vol. 44, pp. 420-421, Mar. 1996.

[18] R. J. Burkholder and T. Lundin, "Forward-backward iterative physical optics algorithm for computing the RCS of open-ended cavities," *IEEE Trans. Antennas Propagat.*, vol. 53, pp. 793-799, Feb. 2005.

[19] R. G. Koujoumijan and P. H. Pathak, "A Uniform geometrical theory of diffraction for an edge in a perfectly conducting surface," *Proc. IEEE*, vol. 62, pp. 1448-1461, Nov. 1974.

[20] J. B. Keller, "Geometrical theory of diffraction," *Journal of the Optical Society of America*, vol. 52, pp. 116-130, 1962.

[21] R. Tiberio, G. Pelosi, and G. Manara, "A uniform GTD formulation for the diffraction by a wedge with impedance faces," *IEEE Trans. Antennas Propagat.*, vol. 33, pp. 867-873, Aug. 1985.

[22] J. L. Volakis, "A uniform geometrical theory of diffraction for an imperfectly conducting half-plane," *IEEE Trans. Antennas Propagat.*, vol. 34, pp. 1172-1180, Feb. 1986.

[23] N. N. Youssef, "Radar cross section of complex targets," *Proceedings of the IEEE*, vol. 77, no. 5, pp. 722-734, May 1989.

Frank Weinmann received the diploma degree in physics from the University of Karlsruhe, Germany, in 1999, and the Dr.-Ing. degree in electrical engineering in 2004 from the same university. From 1999 to 2003, he was with the Institute of Industrial Information Technology, University of Karlsruhe, Germany, where he carried out studies in the field of electromagnetic compatibility of powerline communications, including modelling of radiation sources, propagation mechanisms and regulative aspects. Since 2004 he is with the FGAN-FHR Research Institute for High Frequency Physics and Radar Techniques in Wachtberg, Germany, as a Research Scientist in the Department Antennas and Scattering. His major areas of interest include propagation modeling of microwaves, high-frequency asymptotic techniques, RCS studies, and the design of broad-band planar antennas.